An Adaptive Voltage Control Strategy of Three-Phase Inverter for Standalone Distributed Generation Systems

Ton Duc Do, *Student Member*, Viet Quoc Leu, *Student Member*, Young-Sik Choi, Han Ho Choi, *Member*, *IEEE*, and Jin-Woo Jung, *Member*, *IEEE*

***Abstract*—This paper proposes an adaptive control method of three-phase inverter for standalone distributed generation systems (DGSs). The proposed voltage controller includes two control terms: an adaptive compensating term and a stabilizing term. The adaptive compensating control term is constructed to avoid directly calculating the time derivatives of state variables. Meanwhile, the stabilizing control term is designed to asymptotically stabilize the error dynamics of the system. Also, a fourth-order optimal load current observer is proposed to reduce the number of current sensors and enhance the system reliability and cost effectiveness. Stability of the proposed voltage controller and the proposed load current observer is fully proven by using Lyapunov theory. The proposed control system can establish good voltage regulation such as fast dynamic response, small steady state error, and low total harmonic distortion (THD) under sudden load change, unbalanced load, and nonlinear load. Finally, the validity of the proposed control strategy is verified through simulations and experiments on a prototype DGS test-bed with a TMS320F28335 DSP. For a comparative study, the feedback linearization for multi-input and multi-output (FL-MIMO) control scheme is implemented and its results are presented in this paper.**

***Index Terms*—Adaptive control, distributed generation system (DGS), load current observer, standalone, three-phase inverter, voltage control.**

I. Introduction

Distributed generation systems (DGSs) using renewable energy sources (such as wind turbines, photovoltaic arrays, biomass, fuel cells, etc.) are gaining more and more attention in electric power industry to replace existing fossil fuels and reduce global warming gas emissions. Nowadays, the DGSs are extensively used in grid-connected applications, but they are more economical in a standalone operation in case of rural villages or remote islands because connecting to the grid may lead to higher cost [1]-[5].

In standalone applications, the load-side inverter of the DGS operates analogous to an uninterruptible power supply (UPS) for its local loads [6]. Control of standalone DGSs or UPSs is an attractive research area in recent years. In these applications, the regulation performance of inverter output voltage is evaluated in terms of transient response time, steady state error, and total harmonic distortion (THD). Furthermore, the quality of inverter output voltage is heavily affected by the types of loads such as sudden load change, unbalanced load, and nonlinear load. In [7], a conventional PI controller has been investigated. However, the output voltage has a considerable amount of the steady state error and its THD is not satisfactory in case of nonlinear load. The H_∞ loop-shaping control scheme which is presented in [8] also cannot effectively mitigate the THD of the output voltage under nonlinear load. Therefore, the load-side inverters require advanced control techniques to achieve excellent voltage regulation performance, especially, under sudden load disturbance, unbalanced load, and nonlinear load.

Recently, various advanced control methods are applied to the load-side inverters in DGS and UPS applications [6], [9]-[23]. In [9]-[11], a repetitive control is used to regulate UPS inverters, but the general problem with a repetitive control is its slow response and lack of systematical method to stabilize the error dynamics. Feedback linearization control techniques are proposed in [12], [13]. Although these methods can achieve high performance of the output voltage, the control design techniques seem to be complicated. Two iterative learning control strategies are presented in [14], and these methods are capable of achieving high performance. However, the switching frequency of the inverter is very high, so it results in huge switching losses. In [15], a model predictive control with a load current observer is proposed. Although the control technique is simple, the THD of the output voltage is still high. In [16], another predictive control is proposed, but nonlinear load is not investigated. In [17], a robust PI controller is proposed for an autonomous distributed generation unit. A full set of results are presented in case of unbalanced *RLC* load, but the results about nonlinear load are not presented. Sliding mode control techniques are applied for inverters in [18]-[21]. In [18], the experimental results show that the output voltage THD is still high under nonlinear load. In [19]-[21], although good performance can be obtained, the controller designs are only for single-phase inverters [19], [20] and the results of nonlinear load are not presented [21]. In [6], a robust servomechanism control (RSC) is used to

Manuscript received May 31, 2012; revised September 21, 2012; accepted for publication November 10, 2012. This work was supported by the National Research Foundation of Korea (NRF) grant funded by the Korea government (MEST) (No. 2012R1A2A2A01045312).

The authors are with the Division of Electronics and Electrical Engineering, Dongguk University-Seoul, Seoul 100-715, South Korea (e-mail: jinwjung@dongguk.edu).

control three-phase inverter of a DGS in a standalone mode. Even though this control technique can achieve good performance, it is quite complicated and needs exact parameter values of an *RLC* load. In [22] and [23], the authors propose the control strategies that consist of an RSC in an outer loop and a sliding mode control in an inner loop. Even if the simulation and experimental results show good voltage performance, the control approach is complicated.

This paper proposes an adaptive voltage controller and an optimal load current observer of three-phase inverter for standalone DGSs. Also, it is analytically proven that the proposed voltage controller and the proposed load current observer are asymptotically stable, respectively. The proposed control method can achieve excellent voltage regulation such as fast transient behavior, small steady state error, and low THD under sudden load change, unbalanced load, and nonlinear load. For a comparative study, the feedback linearization for multi-input and multi-output (FL-MIMO) control method in [12] is implemented in this paper. Simulation is done by using Matlab/Simulink software and experiments are carried out on a prototype DGS test-bed with a TMS320F28335 DSP.

The remaining part of this paper is organized as follows. Section II describes the DGS in a standalone operation and the state-space model of the load-side inverter. The design and stability analysis of a proposed adaptive voltage controller are fully addressed in Section III. Section IV illustrates a proposed load current observer and analyzes its stability. In Section V, the simulation and experimental results are given to evaluate the performance of the proposed control algorithm. Finally, conclusions are drawn in Section VI.

II. System Description and Mathematical Model

The configuration of a typical DGS in a standalone operation is illustrated in Fig. 1. It consists of renewable energy sources (e.g., wind turbines, solar cells, and fuel cells), an ac-dc power converter (wind turbines) or a unidirectional dc-dc boost converter (solar cells or fuel cells), a three-phase dc-ac inverter, an *LC* output filter, a DSP control unit, and a local load. As shown in Fig. 1, a transformer can be used to provide an electrical isolation or boost the output voltage of the three-phase inverter, but it may lead to higher cost and larger volume. Also, storage systems such as batteries, ultra-capacitors, and flywheels may be used to generate electric power during the transient (e.g., start-up or sudden load change) and improve the reliability of renewable energy sources.

In this paper, we deal with the voltage controller design of the three-phase inverter for standalone DGSs that can assure excellent voltage regulation (i.e., fast transient response, small steady state error, and low THD) under sudden load change, unbalanced load, and nonlinear load. Thus, renewable energy sources and ac-dc power converter or unidirectional dc-dc boost converter can be replaced with a dc voltage source (V_{dc}). Fig. 2 describes the circuit model of a three-phase inverter with an *LC* output filter for standalone DGSs. As depicted in Fig. 2, the system comprises four parts: a dc voltage source (V_{dc}), a three-phase PWM inverter (S_1 through S_6), an output filter (L_f and C_f), and a three-phase load (R_L). Note that the *LC* filter is required to suppress high-order harmonic components of the inverter output voltage due to the PWM action and then provide the load with sinusoidal voltages.

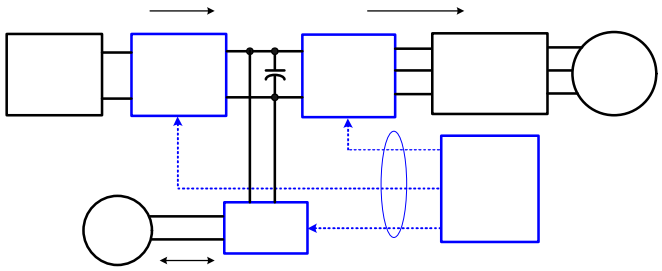

Fig. 1. Configuration of a typical DGS in a standalone operation.

The circuit model in Fig. 2 uses the following quantities. The inverter output line to neutral voltage and phase current vectors are given by $\mathbf{V}_i = [v_{iA}\ v_{iB}\ v_{iC}]^T$ and $\mathbf{I}_i = [i_{iA}\ i_{iB}\ i_{iC}]^T$, respectively. In addition, the load line to neutral voltage and phase current are represented by the vectors $\mathbf{V}_L = [v_{LA}\ v_{LB}\ v_{LC}]^T$, and $\mathbf{I}_L = [i_{LA}\ i_{LB}\ i_{LC}]^T$, respectively.

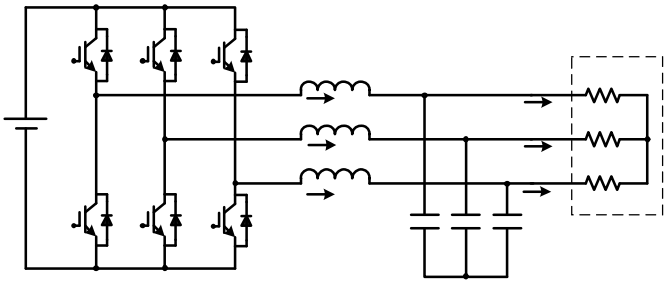

Fig. 2. Circuit diagram of a three-phase inverter with an *LC* output filter for standalone DGSs.

Assume that three-phase voltages and currents used in Fig. 2 are balanced. By applying *Kirchoff's current law* (*KCL*) and *Kirchoff's voltage law* (*KVL*) at the *LC* output filter, the following voltage and current equations can be derived:

$$\begin{cases} \dfrac{d\mathbf{V}_L}{dt} = \dfrac{1}{C_f}\mathbf{I}_i - \dfrac{1}{C_f}\mathbf{I}_L \\ \dfrac{d\mathbf{I}_i}{dt} = \dfrac{1}{L_f}\mathbf{V}_i - \dfrac{1}{L_f}\mathbf{V}_L \end{cases} \tag{1}$$

Under balanced conditions, the above state equations (1) in the stationary *abc* reference frame can be transformed to the equations in the stationary *αβ* reference frame by using the following expression [2]-[3]:

$$\mathbf{X}_{\alpha\beta} = x_a e^{j0} + x_b e^{j\frac{2\pi}{3}} + x_c e^{j\frac{4\pi}{3}} \tag{2}$$

where $\mathbf{X}_{\alpha\beta} = x_\alpha + jx_\beta$.

Thus, the state equations (1) can be transformed to the following:

$$\begin{cases} \dfrac{d\mathbf{V}_{L\alpha\beta}}{dt} = \dfrac{1}{C_f}\mathbf{I}_{i\alpha\beta} - \dfrac{1}{C_f}\mathbf{I}_{L\alpha\beta} \\ \dfrac{d\mathbf{I}_{i\alpha\beta}}{dt} = \dfrac{1}{L_f}\mathbf{V}_{i\alpha\beta} - \dfrac{1}{L_f}\mathbf{V}_{L\alpha\beta} \end{cases} \tag{3}$$

where $\mathbf{V}_{L\alpha\beta} = [v_{L\alpha}\ v_{L\beta}]^T$, $\mathbf{I}_{L\alpha\beta} = [i_{L\alpha}\ i_{L\beta}]^T$, $\mathbf{V}_{i\alpha\beta} = [v_{i\alpha}\ v_{i\beta}]^T$, and $\mathbf{I}_{i\alpha\beta} = [i_{i\alpha}\ i_{i\beta}]^T$.

Next, the state equations in the stationary $\alpha\beta$ reference frame can be transformed to the equations in the synchronously rotating dq reference frame from the following formula:

$$\mathbf{X}_{dq} = x_d + jx_q = \mathbf{X}_{\alpha\beta}e^{-j\theta} \tag{4}$$

where $\theta(t) = \int_0^t \omega(\tau)d\tau + \theta_0$ is the transformation angle, ω is the angular frequency ($\omega = 2\pi \cdot f$), and f is the fundamental frequency of voltage or current.

Finally, the equations (3) can be transformed to

$$\begin{cases} \dfrac{d\mathbf{V}_{Ldq}}{dt} + j\omega\mathbf{V}_{Ldq} = \dfrac{1}{C_f}\mathbf{I}_{idq} - \dfrac{1}{C_f}\mathbf{I}_{Ldq} \\ \dfrac{d\mathbf{I}_{idq}}{dt} + j\omega\mathbf{I}_{idq} = \dfrac{1}{L_f}\mathbf{V}_{idq} - \dfrac{1}{L_f}\mathbf{V}_{Ldq} \end{cases} \tag{5}$$

where $\mathbf{V}_{Ldq} = [v_{Ld}\ v_{Lq}]^T$, $\mathbf{I}_{Ldq} = [i_{Ld}\ i_{Lq}]^T$, $\mathbf{V}_{idq} = [v_{id}\ v_{iq}]^T$, and $\mathbf{I}_{idq} = [i_{id}\ i_{iq}]^T$.

Also, (5) can be rewritten as follows:

$$\begin{cases} \dot{v}_{Ld} = \omega v_{Lq} - \dfrac{1}{C_f}i_{Ld} + \dfrac{1}{C_f}i_{id} \\ \dot{v}_{Lq} = -\omega v_{Ld} - \dfrac{1}{C_f}i_{Lq} + \dfrac{1}{C_f}i_{iq} \\ \dot{i}_{id} = -\dfrac{1}{L_f}v_{Ld} + \omega i_{iq} + \dfrac{1}{L_f}v_{id} \\ \dot{i}_{iq} = -\dfrac{1}{L_f}v_{Lq} - \omega i_{id} + \dfrac{1}{L_f}v_{iq} \end{cases} \tag{6}$$

where $\dot{v}_{Ld}$, $\dot{v}_{Lq}$, $\dot{i}_{id}$, and $\dot{i}_{iq}$ denote the time derivatives of v_{Ld}, v_{Lq}, i_{id}, and i_{iq}, respectively.

Note that $\mathbf{V}_{Ldq}$ and $\mathbf{I}_{idq}$ are the state variables, $\mathbf{V}_{idq}$ is the control input, and $\mathbf{I}_{Ldq}$ is defined as the disturbance.

In this paper, the following assumptions are made to design an adaptive controller and a load current observer:

1) v_{Ld}, v_{Lq}, i_{id}, and i_{iq} are available.
2) The desired load dq-axis voltages v_{Ldref} and v_{Lqref} are constant, and its derivatives can be set to zero.
3) i_{Ld} and i_{Lq} are unknown, and they change very slowly during the sampling period [15].

III. Adaptive Voltage Controller Design and Stability Analysis

Based on the system model (6), this section fully addresses the proposed adaptive control algorithm and its stability analysis.

First, the errors of the load dq-axis voltages (v_{Ld} and v_{Lq}) and the inverter dq currents (i_{id} and i_{iq}) can be defined as

$$\begin{aligned} &\bar{v}_{Ld} = v_{Ld} - v_{Ldref}, \quad \bar{v}_{Lq} = v_{Lq} - v_{Lqref} \\ &\bar{i}_{id} = i_{id} - i_{idref}, \quad \bar{i}_{iq} = i_{iq} - i_{iqref} \end{aligned} \tag{7}$$

where v_{Ldref} and v_{Lqref} are the reference values of v_{Ld} and v_{Lq}, and i_{idref} and i_{iqref} are the reference values of i_{id} and i_{iq}. Again, the i_{idref} and i_{iqref} are given by

$$i_{idref} = i_{Ld} - \omega C_f v_{Lq}, \quad i_{iqref} = i_{Lq} + \omega C_f v_{Ld} \tag{8}$$

Next, the uncertainty terms u_d and u_q, which cannot be accurately computed in real system, can be defined as

$$\begin{cases} u_d = -\dfrac{\omega L_f}{\alpha_d}v_{Lq} + \dfrac{L_f}{C_f\alpha_d}i_{Ld} - \dfrac{L_f}{C_f\alpha_d}i_{id} \\ \qquad - L_f\omega i_{iq} + L_f\dot{i}_{idref} \\ u_q = \dfrac{\omega L_f}{\alpha_q}v_{Ld} + \dfrac{L_f}{C_f\alpha_q}i_{Lq} + L_f\omega i_{id} \\ \qquad - \dfrac{L_f}{C_f\alpha_q}i_{iq} + L_f\dot{i}_{iqref} \end{cases} \tag{9}$$

where α_d and α_q are positive numbers.

As shown in (9), it should be noted that u_d and u_q include the time derivatives $\dot{i}_{idref}$ and $\dot{i}_{iqref}$ which cannot be calculated directly because they are very noisy. In addition, assume that L_f has some uncertainties due to nonlinear magnetic properties. Therefore, the uncertainty terms u_d and u_q need to be correctly estimated in real time instead of straightforwardly computing the time derivatives of i_{idref} and i_{iqref}.

Then, the following error dynamics can be obtained

$$\begin{cases} \dot{\bar{v}}_{Ld} = \dfrac{1}{C_f}\bar{i}_{id} \\ \dot{\bar{v}}_{Lq} = \dfrac{1}{C_f}\bar{i}_{iq} \\ \dot{\bar{v}}_{Ld} + \alpha_d\dot{\bar{i}}_{id} = -\dfrac{\alpha_d}{L_f}(u_d - v_{id} + v_{Ld}) \\ \dot{\bar{v}}_{Lq} + \alpha_q\dot{\bar{i}}_{iq} = -\dfrac{\alpha_q}{L_f}(u_q - v_{iq} + v_{Lq}) \end{cases} \tag{10}$$

The control inputs v_{id} and v_{iq} can be divided into the following two control terms:

$$\begin{cases} v_{id} = u_{ffd} + u_{fbd} \\ v_{iq} = u_{ffq} + u_{fbq} \end{cases} \tag{11}$$

where u_{ffd} ($= u_d + v_{Ld}$) and u_{ffq} ($= u_q + v_{Lq}$) are the d-axis and q-axis compensation control terms, and u_{fbd} and u_{fbq} are the d-axis and q-axis feedback control terms to stabilize the error dynamics of the system.

In order to establish this estimation law, let the following lemma be considered:

Lemma 1: Assume that ($L_f\dot{i}_{idref} + L_f i_{Ld}/C_f\alpha_d$) and ($L_f\dot{i}_{iqref} + L_f i_{Lq}/C_f\alpha_q$) slowly vary, so they can be set to the constant. There exist constant parameter vectors $m^*_d = [m^*_{d1}, m^*_{d2}, m^*_{d3}, m^*_{d4}]^T$ and $m^*_q = [m^*_{q1}, m^*_{q2}, m^*_{q3}, m^*_{q4}]^T$ such that

$$p_d^T m_d^* = \sum_{i=1}^{4} p_{di}m_{di}^* = u_d, \quad p_q^T m_q^* = \sum_{i=1}^{4} p_{qi}m_{qi}^* = u_q \tag{12}$$

where $p_d = [p_{d1}, p_{d2}, p_{d3}, p_{d4}]^T = [v_{Lq}, i_{id}, i_{iq}, 1]^T$ and $p_q = [p_{q1}, p_{q2}, p_{q3}, p_{q4}]^T = [v_{Ld}, i_{id}, i_{iq}, 1]^T$.

Proof: It is clear that (12) holds with

$$m_d^* = \left[-\frac{\omega L_f}{\alpha_d}, \quad -\frac{L_f}{C_f \alpha_d}, \quad -\omega L_f, \quad L_f \dot{i}_{idref} + \frac{L_f}{C_f \alpha_d} i_{Ld} \right]^T$$

$$m_q^* = \left[\frac{\omega L_f}{\alpha_q}, \quad \omega L_f, \quad -\frac{L_f}{C_f \alpha_q}, \quad L_f \dot{i}_{iqref} + \frac{L_f}{C_f \alpha_q} i_{Lq} \right]^T \tag{13}$$

■

Therefore, the following theorem can be established.

Theorem 1: Assume that C_f is known. Let the compensation control terms (u_{ffd} and u_{ffq}) and the feedback control terms (u_{fbd} and u_{fbq}) be calculated by the following adaptive control laws:

$$\begin{cases} u_{ffd} = \sum_{i=1}^{4} m_{di} p_{di} + v_{Ld}, \quad u_{fbd} = -\delta_d \sigma_d \\ u_{ffq} = \sum_{i=1}^{4} m_{qi} p_{qi} + v_{Lq}, \quad u_{fbq} = -\delta_q \sigma_q \end{cases} \tag{14}$$

where

$$m_{di} = -\frac{1}{\phi_{di}} \int_0^t p_{di} \sigma_d d\tau, \quad m_{qi} = -\frac{1}{\phi_{qi}} \int_0^t p_{qi} \sigma_q d\tau \tag{15}$$

$$\sigma_d = (\bar{v}_{Ld} + \alpha_d \bar{i}_{id}), \quad \sigma_q = (\bar{v}_{Lq} + \alpha_d \bar{i}_{iq}) \tag{16}$$

and α_d and α_q are positive design constants, m_{di} and m_{qi} are estimates of m^*_{di} and m^*_{qi}, $\delta_d > 0$, $\delta_q > 0$, $\phi_{di} > 0$, $\phi_{qi} > 0$. Then $\bar{v}_{Ld}$ and $\bar{v}_{Lq}$ converge to zero, and m_{di} and m_{qi} are bounded.

Proof: Let the Lyapunov function be defined as

$$V(t) = \sigma_d^2 + \sigma_q^2 + \sum_{i=1}^{4} \frac{\alpha_d}{L_f} \phi_{di} \bar{m}_{di}^2 + \sum_{i=1}^{4} \frac{\alpha_q}{L_f} \phi_{qi} \bar{m}_{qi}^2 \tag{17}$$

where $\bar{m}_{di} = m^*_{di} - m_{di}$ and $\bar{m}_{qi} = \xi^*_{qi} - \xi_{qi}$. Its time derivative is expressed as the following

$$\dot{V} = 2(\sigma_d \dot{\sigma}_d + \sigma_q \dot{\sigma}_q - \sum_{i=1}^{4} \frac{\alpha_d}{L_f} \phi_{di} \bar{m}_{di} \dot{m}_{di} - \sum_{i=1}^{4} \frac{\alpha_q}{L_f} \phi_{qi} \bar{m}_{qi} \dot{m}_{qi}) \tag{18}$$

Also, the following equation can be obtained from (10) and (16)

$$\begin{cases} \dot{\sigma}_d = \frac{\alpha_d}{L_f}(v_{id} - u_d - v_{Ld}) \\ \dot{\sigma}_q = \frac{\alpha_q}{L_f}(v_{iq} - u_q - v_{Lq}) \end{cases} \tag{19}$$

On the other hand, *Lemma 1*, (11), (14) and (15) imply that

$$\begin{cases} v_{id} = -\delta_d \sigma_d + v_{Ld} - \sum_{i=1}^{4} \bar{m}_{di} p_{di} + u_d \\ v_{iq} = -\delta_q \sigma_q + v_{Lq} - \sum_{i=1}^{4} \bar{m}_{qi} p_{qi} + u_q \end{cases}$$

$$\begin{cases} \dot{m}_{di} = -\frac{1}{\phi_{di}} p_{di} \sigma_d \\ \dot{m}_{qi} = -\frac{1}{\phi_{qi}} p_{qi} \sigma_q \end{cases} \tag{20}$$

where the following equalities are used

$$\sum_{i=1}^{4} m_{di} p_{di} = u_d - \sum_{i=1}^{4} \bar{m}_{di} p_{di}, \quad \sum_{i=1}^{4} m_{qi} p_{qi} = u_q - \sum_{i=1}^{4} \bar{m}_{qi} p_{qi}$$

Substituting (19) and (20) into (17) yields

$$\dot{V} = -2\left(\delta_d \frac{\alpha_d}{L_f} \sigma_d^2 + \delta_q \frac{\alpha_q}{L_f} \sigma_q^2 \right) \le 0 \tag{21}$$

Integrating both sides of (20) gives

$$\int_0^\infty \dot{V}(\tau) d\tau \le -2\left(\delta_d \frac{\alpha_d}{L_f} \int_0^\infty \sigma_d^2 d\tau + \delta_q \frac{\alpha_q}{L_f} \int_0^\infty \sigma_q^2 d\tau \right)$$

or equivalently

$$V(\infty) - V(0) \le -2\left(\delta_d \frac{\alpha_d}{L_f} \int_0^\infty \sigma_d^2 d\tau + \delta_q \frac{\alpha_q}{L_f} \int_0^\infty \sigma_q^2 d\tau \right) \tag{22}$$

Thus, the above equation can be rewritten as

$$2\left(\delta_d \frac{\alpha_d}{L_f} \int_0^\infty \sigma_d^2 d\tau + \delta_q \frac{\alpha_q}{L_f} \int_0^\infty \sigma_q^2 d\tau \right) \le V(0) - V(\infty) \le V(0) \tag{23}$$

where $V(t) \ge 0$ is used. Then, the following inequalities can be derived:

$$\int_0^\infty \sigma_d^2 d\tau < \infty, \qquad \int_0^\infty \sigma_q^2 d\tau < \infty \tag{24}$$

which implies that σ_d, $\sigma_q \in L_2$. Since $\dot{V} \le 0$ as shown in (21), $V(t)$ is nonincreasing and is upper bounded as $V(t) \le V(0)$. This implies that $\sigma_d \in L_\infty$, $\sigma_q \in L_\infty$, $m_{qi} \in L_\infty$, $m_{qi} \in L_\infty$.

Meanwhile, from first two equations of (10), the σ_d and σ_q given in (16) can be rearranged as

$$\begin{cases} \sigma_d = (\bar{v}_{Ld} + C_f \alpha_d \dot{\bar{v}}_{Ld}) \\ \sigma_q = (\bar{v}_{Lq} + C_f \alpha_q \dot{\bar{v}}_{Lq}) \end{cases} \tag{25}$$

Then, the transfer functions $H_d(s)$ from σ_d to $\bar{v}_{Ld}$ and $H_q(s)$ from σ_q to $\bar{v}_{Lq}$ are given by the following strictly positive functions:

$$H_d(s) = \frac{1}{(1 + C_f \alpha_d s)}, \; H_q(s) = \frac{1}{(1 + C_f \alpha_q s)} \tag{26}$$

Therefore, by [24] it can be concluded that $\bar{v}_{Ld}$ and $\bar{v}_{Lq}$ converge to zero. ■

Remark 1: This remark discusses how the controller gains are chosen. The adaptive gains m_{di} and m_{qi} are incorporated in the compensation control terms u_{ffd} and u_{ffq} as depicted in (14). To realize the fast convergence and transient response, the adaptive gains are tuned to large values. Since these adaptive gains are inversely related to ϕ_{di} and ϕ_{qi} as in (15), the smaller values selected for ϕ_{di} and ϕ_{qi}, the more likely to result in larger values of the adaptive gains. On the other hand, with the feedback terms u_{fbd} and u_{fbq} given in (14), σ_d and σ_q are

further defined in (25), and these feedback terms can be regarded as a PD controller. In this context, the control parameters α_d, α_q, δ_d, and δ_q can be decided based on the tuning rule of [25]. Finally, the parameters α_d, α_q, δ_d, δ_q, ϕ_{di}, and ϕ_{qi} can be tuned by the following procedure: 1) By utilizing the tuning rule of [25], the parameters α_d, α_q, δ_d, and δ_q are tuned; 2) Set quite large values for ϕ_{di} and ϕ_{qi}; 3) Reduce ϕ_{di} and ϕ_{qi} by a small amount; 4) If the acceptable transient performance is attained by current control parameters, then it is done. Otherwise, return to step 3 above.

Remark 2: As shown in (14), the proposed voltage controller includes two parts: feedback terms and adaptive compensation terms. The function of the feedback terms is to stabilize the error dynamics of the system. On separate note, the adaptive compensation terms take into accounts not only parameter uncertainties but also noises. Therefore, the proposed control technique can attain good performance with the existence of parameter uncertainties and noises in practice.

Fig. 3 depicts the block diagram of the proposed adaptive voltage control scheme.

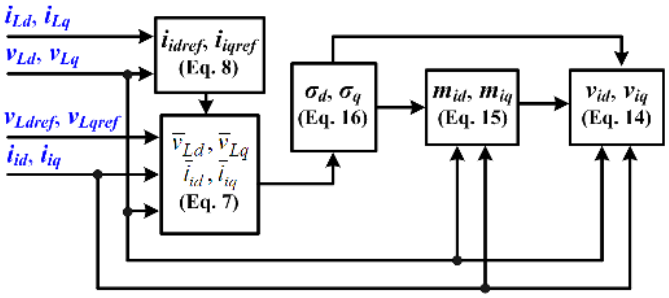

Fig. 3. Block diagram of the proposed adaptive voltage control scheme.

IV. Load Current Observer Design and Stability Analysis

In Fig. 3, it is clear that the proposed adaptive controller needs load current information. Using the current sensors to measure the load currents ($\mathbf{I}_L$) makes the system more expensive and less reliable. In this section, a linear optimal load current observer is designed to accurately estimate load current information that can heavily affect the controller performance. Based on *assumption* 3 and first two equations of (6), a fourth-order dynamic model can be obtained as follows:

$$\dot{x} = Ax + Bu \tag{27}$$

where

$$x = \begin{bmatrix} i_{Ld} \\ i_{Lq} \\ v_{Ld} \\ v_{Lq} \end{bmatrix}, A = \begin{bmatrix} 0 & 0 & 0 & 0 \\ 0 & 0 & 0 & 0 \\ -1/C_f & 0 & 0 & \omega \\ 0 & -1/C_f & -\omega & 0 \end{bmatrix},$$

$$B = \begin{bmatrix} 0 & 0 \\ 0 & 0 \\ 1/C_f & 0 \\ 0 & 1/C_f \end{bmatrix}, u = \begin{bmatrix} i_{id} \\ i_{iq} \end{bmatrix}$$

Then, the load current observer model can be represented as

$$\begin{aligned} \dot{\hat{x}} &= A\hat{x} + My - MC\hat{x} + Bu \\ y &= Cx \\ \hat{\mathbf{I}}_{Ldq} &= \begin{bmatrix} \hat{i}_{Ld} \\ \hat{i}_{Lq} \end{bmatrix} = C_T \hat{x} \end{aligned} \tag{28}$$

where $\hat{i}_{Ld}$ and $\hat{i}_{Lq}$ are estimates of i_{Ld} and i_{Lq}, $M \in R^{4\times 2}$ is an observer gain matrix, and

$$\hat{x} = \begin{bmatrix} \hat{i}_{Ld} \\ \hat{i}_{Lq} \\ \hat{v}_{Ld} \\ \hat{v}_{Lq} \end{bmatrix}, C = \begin{bmatrix} 0 & 0 & 1 & 0 \\ 0 & 0 & 0 & 1 \end{bmatrix}, C_T = \begin{bmatrix} 1 & 0 & 0 & 0 \\ 0 & 1 & 0 & 0 \end{bmatrix}$$

Fig. 4 illustrates the block diagram of the proposed load current observer.

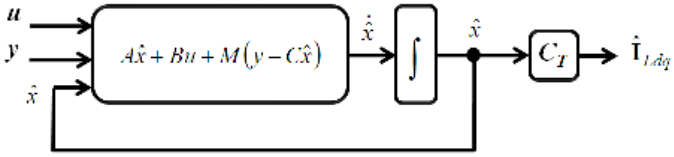

Fig. 4. Block diagram of the proposed optimal load current observer.

Next, the error dynamics of the load current observer can be obtained as follows:

$$\dot{\tilde{x}} = (A - MC)\tilde{x} \tag{29}$$

where $\tilde{x} = x - \hat{x}$.

Theorem 2: Consider the following algebraic Riccati equation (ARE)

$$AP + PA^T - PC^T R^{-1} CP + Q = 0 \tag{30}$$

where $Q \in R^{4\times 4}$ is a symmetric positive semidefinite matrix, $R \in R^{2\times 2}$ is a symmetric positive definite matrix, and $P \in R^{4\times 4}$ is a solution matrix. Also, assume that the load current observer gain matrix M is given by

$$M = PC^T R^{-1} \tag{31}$$

Then, the estimation error converges exponentially to zero.

Proof: Let us define the Lyapunov function as $V_o(\tilde{x}) = \tilde{x}^T X \tilde{x}$, where $X = P^{-1}$. Its time derivative along the error dynamics (29) is given by

$$\begin{aligned} \dot{V}_o(\tilde{x}) &= \frac{d}{dt}\tilde{x}^T X\tilde{x} = 2\tilde{x}^T \left(XA - XPC^T R^{-1} C\right)\tilde{x} \\ &= \tilde{x}^T X\left(AP + PA^T - 2PC^T R^{-1} CP\right)X\tilde{x} \le -\tilde{x}^T XQX\tilde{x} \end{aligned} \tag{32}$$

This implies that $\tilde{x}$ is exponentially stable.

Remark 3: The proposed fourth-order load current observer is the Kalman-Bucy optimal observer which minimizes the performance index $E(\tilde{x}^T\tilde{x})$ representing the expectation value of $\tilde{x}^T\tilde{x}$ for the following perturbed model

$$\dot{x} = Ax + Bu + d, \quad y = Cx + v \tag{33}$$

where $d \in R^4$, $v \in R^2$ are independent white Gaussian noise signals with $E(d) = 0$, $E(v) = 0$, $E(dd^T) = Q$, and $E(vv^T) = R$.

Remark 4: By referring to [26], this remark details on how the observer gain matrix M is determined. Normally, the observer performance is mostly influenced by the system model if the measurements are excessively noisy (R large) and the input noise intensity is small (Q small). On that note, M is small. This leads to a slow observer as measured by the location of its eigenvalues. However, if the measurements are good and the input noise intensity is large, the observer relies on the measurement. In this case, M is large, resulting in a fast observer with high bandwidth. Consequently, by assuming that the measurement is good, the fast observer is desirable. Lastly, the subsequent procedure summarizes the tuning process of the observer gain matrix M: 1) Q and R are set as identity matrices; 2) Gradually, increase Q and decrease R, then calculate M as in (30) and (31); 3) Unless the observer performance is satisfied, return to step 2 above. Otherwise, quit.

V. Performance Evaluation

In this section, simulations and experiments are made and various results are presented. To evaluate the performance of the proposed observer-based adaptive control system, two kinds of power levels (200 kVA class and 450 VA class) are studied because the 200 kVA unit is too high a power level to build in the laboratory. In this paper, simulations are performed by using Matlab/Simulink software and experiments are implemented on a prototype DGS test-bed with a TMS320F28335 DSP.

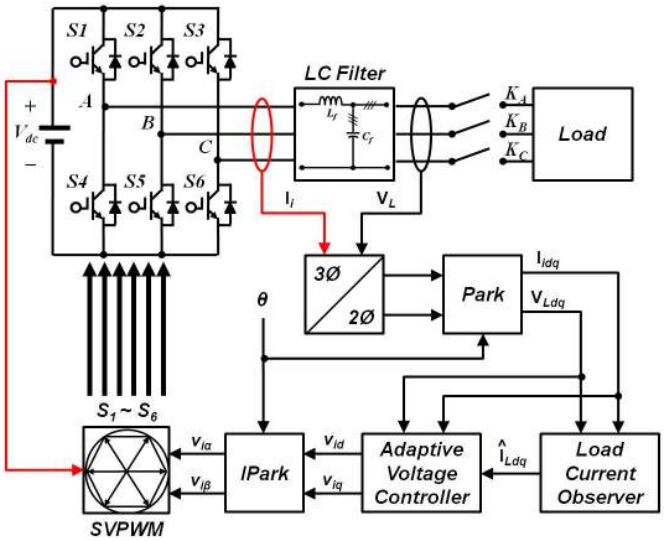

Fig. 5. Overall block diagram of the proposed adaptive control system.

Fig. 5 shows the schematic diagram of the proposed adaptive voltage control approach. As depicted in Fig. 5, the inverter currents ($\mathbf{I}_i$) and load output voltages ($\mathbf{V}_L$) are measured with sensors and then transformed to the quantities ($\mathbf{I}_{idq}$, $\mathbf{V}_{Ldq}$) in the synchronously rotating dq reference frame, respectively. On the other hand, the load currents ($\mathbf{I}_{Ldq}$) can be estimated by using the proposed current observer. In this paper, a space-vector pulse-width modulation (SVPWM) technique is utilized to approximate the reference voltages and supply less harmonic voltages to the load. Simulations and experiments are accomplished to demonstrate the transient and steady state performances of the proposed control algorithm under the following four different cases:

- **Case 1**: Balanced resistive load (Transient behavior - 0% to 100%)
- **Case 2**: Balanced resistive load (Transient behavior - 100% to 0%)
- **Case 3**: Unbalanced resistive load (phase C opened)
- **Case 4**: Nonlinear load (A three-phase diode rectifier)

Fig. 6 illustrates a nonlinear load circuit that consists of a three-phase full-bridge diode rectifier, an inductor (L_{load}), a capacitor (C_{load}), and a resistor (R_{load}).

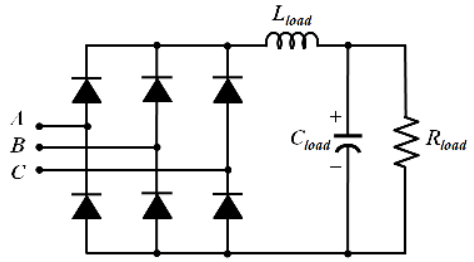

Fig. 6. Nonlinear load circuit with a three-phase diode rectifier.

A. 200 kVA Unit

Consider a 200 kVA DG unit and the system parameters are given in Table I.

TABLE I
System Parameters of a 200 kVA Unit

DGS rated power	200 kVA
dc-link voltage (V_{dc})	600 V
Switching & sampling frequency	4 kHz
Load output voltages ($\mathbf{V}_{L,\,rms}$)	220 V
Fundamental frequency (f)	60 Hz
Output filter capacitance (C_f)	500 μF
Output filter inductance (L_f)	0.3 mH

As shown in Table I, a three-phase LC output filter is designed with L_f = 0.3 mH and C_f = 500 μF, and it has a cut-off frequency of 410.9 Hz. It is well known that the larger the values of L_f and C_f, the better filter performance. However, large L_f leads to higher cost and larger volume. Also, large C_f results in larger capacitor current at no load besides higher cost. Therefore, there exists a trade-off when selecting L_f and C_f.

In this case, the controller gains and observer gain matrix are selected as follows: $\alpha_d = \alpha_q = 0.1$, $\phi_{di} = \phi_{qi} = 1000$, $\delta_d = \delta_q = 1000$, and

$$M = 10^4 \times \begin{bmatrix} -0.3162 & -0.0039 & 3.0955 & -0.0000 \\ 0.0039 & -0.3162 & -0.0000 & 3.0955 \end{bmatrix}^T$$

Note that these parameters are chosen through extensive simulation studies with the aforementioned procedures in *Remark 1* and *Remark 4*.

Figs. 7 to 10 show the simulation results of the proposed control technique under Cases 1 to 4 for a 200 kVA unit, respectively. Each figure shows the waveforms of load voltages ($\mathbf{V}_L$), inverter currents ($\mathbf{I}_i$), load currents ($\mathbf{I}_L$),

estimated load currents ($\hat{\mathbf{I}}_L$), control inputs (v_{id}, v_{iq}), and load current error ($e_{LA} = i_{LA} - \hat{i}_{LA}$). In Figs. 7 to 9, a 0.726 Ω resistor is used for a balanced resistive load and an unbalanced resistive load. Also, to get the waveforms under nonlinear load in Fig. 10, the following values are chosen: L_{load} = 0.3 mH, C_{load} = 4000 μF, and R_{load} = 1.2 Ω. Figs. 7 and 8 show the transient performance under a balanced resistive load and the load voltage waveforms are only slightly distorted during the transients and return to steady state within 0.52 ms. Figs. 9 and 10 show the steady state performance under an unbalanced resistive load and a nonlinear load, respectively. In both figures, the voltage waveforms look quite sinusoidal throughout the time. In Figs. 7 through 10, it is seen that the proposed observer accurately estimates the load currents under four load scenarios.

Table II presents the steady state performance of the simulation results under four different loads for a 200 kVA unit. It can be observed from Table II that the steady state errors are smaller than 0.31% and the THDs of the output voltages are lower than 0.8% in all cases.

TABLE II
STEADY-STATE PERFORMANCE OF SIMULATION RESULTS FOR A 200 KVA UNIT WITH PROPOSED CONTROL SCHEME

Load Types	Load Output Voltages (V_{rms})			THD (%)
	v_{LA}	v_{LB}	v_{LC}	
Balanced resistive load	219.88	219.86	219.85	0.211
Unbalanced *A*&*B* resistive load	220.17	219.94	219.65	0.208
No load	219.89	219.84	219.86	0.224
Nonlinear load (Crest factor 1.37:1)	219.57	219.45	219.32	0.781

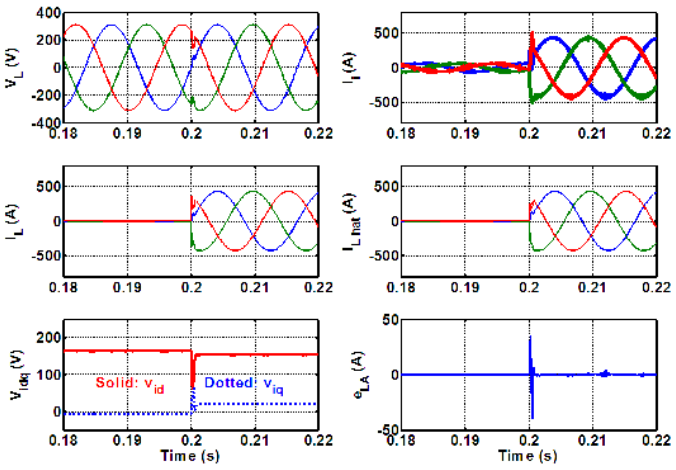

Fig. 7. Simulation results of the proposed control scheme under Case 1 for a 200 kVA unit (Balanced resistive load: 0% to 100%).

B. 450 VA Unit

To testify the performance of the proposed control algorithm, the power size is reduced to 450 VA in the laboratory. Accordingly, for comparison, the simulation and experimental results are illustrated in this subsection. Table III shows the system parameters of a 450 VA unit. As listed in Table III, a three-phase *LC* output filter is chosen with L_f = 10 mH and C_f = 6.67 μF, and this filter has a natural frequency (ω_c) of 3872 rad/s. In this case, the controller gains and observer gain matrices are chosen as follows: $\alpha_d = \alpha_q = 20$, $\phi_{di} = \phi_{qi} = 100$, $\delta_d = \delta_q = 100$, and

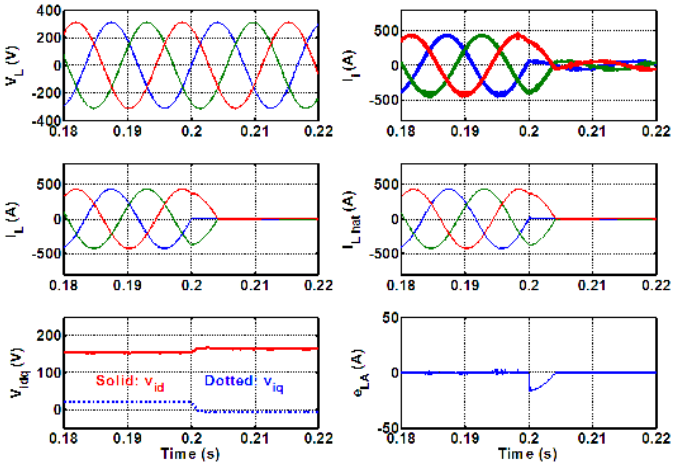

Fig. 8. Simulation results of the proposed control scheme under Case 2 for a 200 kVA unit (Balanced resistive load: 100% to 0%).

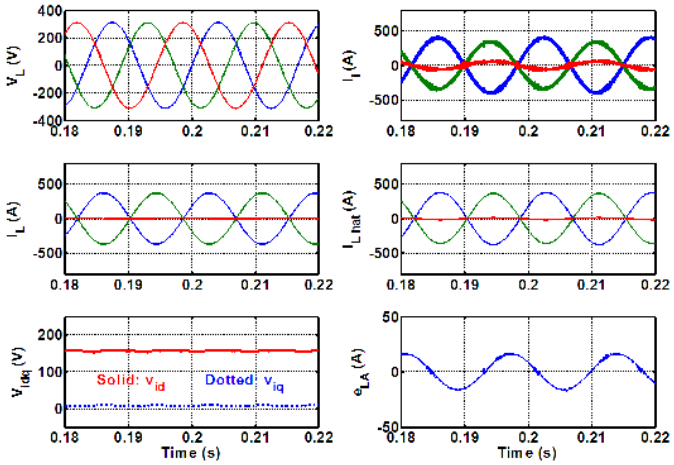

Fig. 9. Simulation results of the proposed control scheme under Case 3 for a 200 kVA unit (Unbalanced resistive load: phase *C* opened).

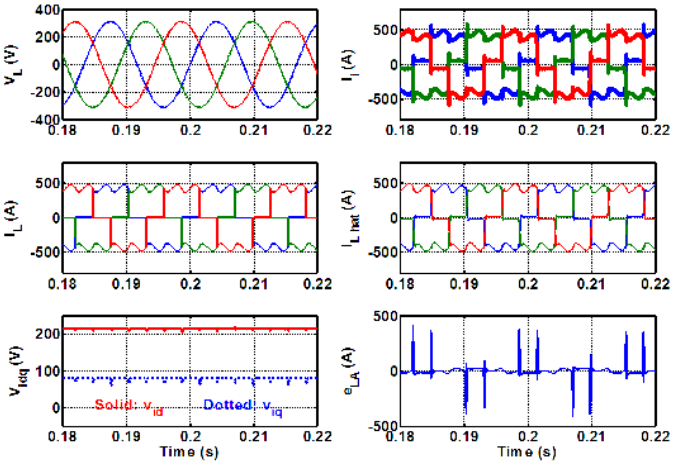

Fig. 10. Simulation results of the proposed control scheme under Case 4 for a 200 kVA unit (Nonlinear load with crest factor 1.37:1).

$$M = 10^4 \times \begin{bmatrix} -0.1000 & -0.0022 & 1.7406 & -0.0000 \\ 0.0022 & -0.1000 & -0.0000 & 1.7406 \end{bmatrix}^T$$

Figs. 11 to 14 show the simulation results of the proposed control method under Cases 1 to 4 for a 450 VA unit, respectively. Figs. 15 to 18 show the experimental results under the same conditions as Figs. 11 to 14, respectively. Each figure shows the waveforms of load voltages ($\mathbf{V}_L$), inverter currents ($\mathbf{I}_i$), load currents ($\mathbf{I}_L$), estimated load currents ($\hat{\mathbf{I}}_L$), control inputs (v_{id}, v_{iq}), and load current error ($e_{LA} = i_{LA} - \hat{i}_{LA}$). It is noted that a 80 Ω resistor is given as a balanced resistive load and an unbalanced resistive load, while the following *RLC* values are used in a nonlinear load circuit shown in Fig. 6: L_{load} = 10 mH, C_{load} = 680 μF, and R_{load} = 200 Ω.

TABLE III
SYSTEM PARAMETERS OF A 450 VA UNIT

DGS rated power	450 VA
dc-link voltage (V_{dc})	280 V
Switching & sampling frequency	5 kHz
Load output voltages ($\mathbf{V}_{L,\,rms}$)	110 V
Fundamental frequency (f)	60 Hz
Output filter capacitance (C_f)	6.67 μF
Output filter inductance (L_f)	10 mH

Figs. 11 and 12 show the simulation results of the transient performances under a balanced resistive load. In these figures, the load voltage waveforms are slightly dented during the transients and are resumed to steady state within 0.5 ms. Meanwhile, the experimental results of Figs. 15 and 16 show that the load voltages are restored to steady state within a short time of 0.6 ms.

Figs. 13, 14, 17, and 18 show the steady state performances of the simulation and experimental results under an unbalanced resistive load and a nonlinear load, respectively. In these figures, the distortions of the voltage waveforms are not found. Based on Figs. 11 through 18, it can be seen that the load currents are precisely estimated by the proposed observer in case of four different loads.

Table IV summarizes the steady-state rms values and THDs of the load voltages in both simulation and experimental results under four different loads for a 450 VA unit. It can be observed from Table IV that the steady state errors are smaller than 0.6% (0.34% in simulations and 0.55% in experiments) and the THDs of the load voltage waveforms are lower than 1.2% (0.405% in simulations and 1.15% in experiments).

For further comparison, the feedback linearization for multi-input and multi-output (FL-MIMO) control scheme in [12] is also implemented in both simulation and experiment studies. Table V sums up the steady-state rms values and THDs of the load voltages in simulation and experimental results under four different loads for a 450 VA unit. In this table, the steady-state errors of the FL-MIMO method are as small as those of the proposed method: 0.30% in simulations and 0.70% in experiments. However, the THDs of the FL-MIMO scheme are much higher than those of the proposed scheme: 0.815%/0.405% in simulations and 2.31%/1.15% in experiments. Figs. 19 and 20 show the simulation and experimental results of the FL-MIMO control method under Case 4, respectively. In this paper, the results of Case 1, 2, 3 are not shown because of the limited space. It should be noted that the FL-MIMO control scheme does not need load current information, so the estimated load currents ($\hat{\mathbf{I}}_L$) and the load current error ($e_{LA} = i_{LA} - \hat{i}_{LA}$) are not available.

TABLE IV
STEADY-STATE PERFORMANCES OF SIMULATION AND EXPERIMENTAL RESULTS FOR A 450 VA UNIT WITH PROPOSED CONTROL SCHEME

Simulation Results				
Load Types	Load rms Output Voltages (V)			THD (%)
	v_{LA}	v_{LB}	v_{LC}	
Balanced resistive load	109.72	109.72	109.72	0.094
Unbalanced *A*&*B* resistive load	109.90	109.75	109.52	0.080
No load	109.80	109.76	109.72	0.095
Nonlinear load (Crest factor 1.59:1)	109.52	109.51	109.52	0.405
Experimental Results				
Load Types	Load rms Output Voltages (V)			THD (%)
	v_{LA}	v_{LB}	v_{LC}	
Balanced resistive load	109.67	109.63	109.72	0.46
Unbalanced *A*&*B* resistive load	109.85	109.64	110.22	0.43
No load	110.17	109.83	110.24	0.51
Nonlinear load (Crest factor 1.52:1)	109.87	109.39	109.64	1.15

TABLE V
STEADY-STATE PERFORMANCES OF SIMULATION AND EXPERIMENTAL RESULTS FOR A 450 VA UNIT WITH FL-MIMO CONTROL METHOD

Simulation Results				
Load Types	Load rms Output Voltages (V)			THD (%)
	v_{LA}	v_{LB}	v_{LC}	
Balanced resistive load	109.85	109.81	109.79	0.418
Unbalanced *A*&*B* resistive load	109.77	109.94	109.67	0.431
No load	109.99	109.87	110.21	0.442
Nonlinear load (Crest factor 1.59:1)	109.76	109.82	109.88	0.815
Experimental Results				
Load Types	Load rms Output Voltages (V)			THD (%)
	v_{LA}	v_{LB}	v_{LC}	
Balanced resistive load	109.74	109.87	109.53	0.75
Unbalanced *A*&*B* resistive load	109.85	109.79	110.73	0.82
No load	110.35	109.79	109.94	0.89
Nonlinear load (Crest factor 1.52:1)	109.90	109.67	109.23	2.31

From all simulation and experimental results, it can be concluded that the proposed control technique can attain exceptional voltage regulation performance such as more stable output voltage and lower THD than the FL-MIMO control method under various load types.

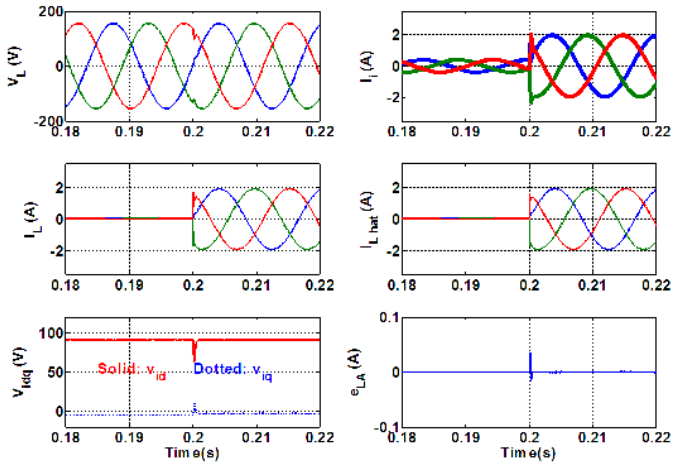

Fig. 11. Simulation results of the proposed control scheme under Case 1 for a 450 VA unit (Balanced resistive load: 0% to 100%).

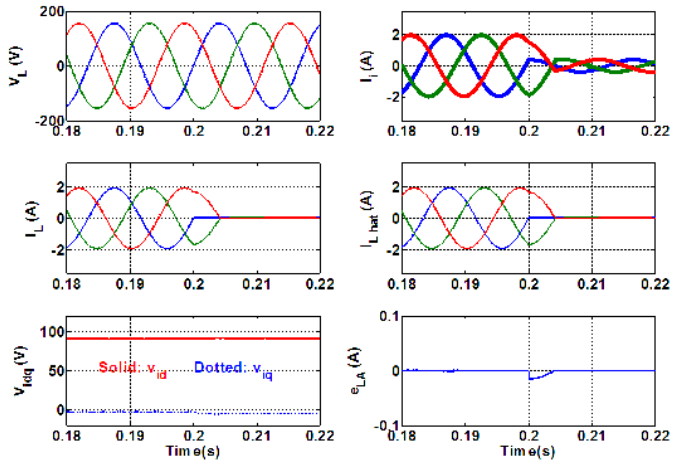

Fig. 12. Simulation results of the proposed control scheme under Case 2 for a 450 VA unit (Balanced resistive load: 100% to 0%).

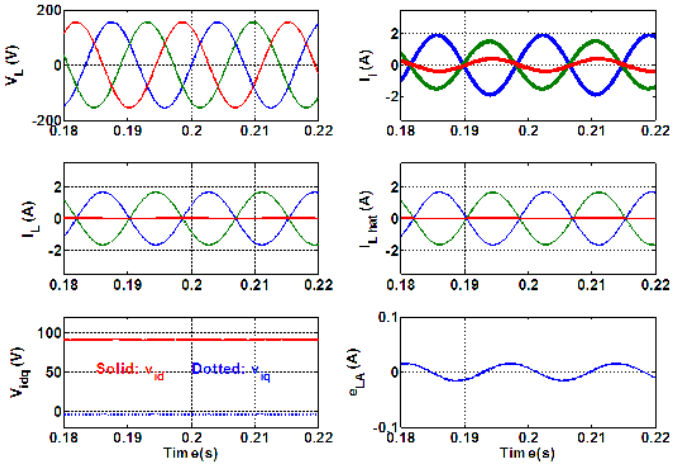

Fig. 13. Simulation results of the proposed control scheme under Case 3 for a 450 VA unit (Unbalanced resistive load: phase *C* opened).

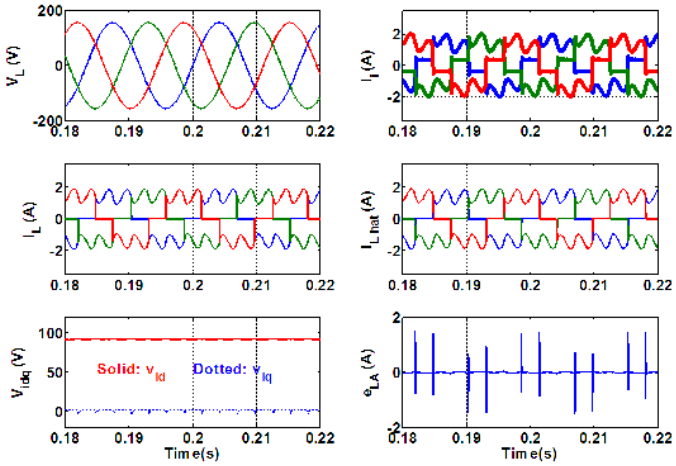

Fig. 14. Simulation results of the proposed control scheme under Case 4 for a 450 VA unit (Nonlinear load with crest factor 1.59:1).

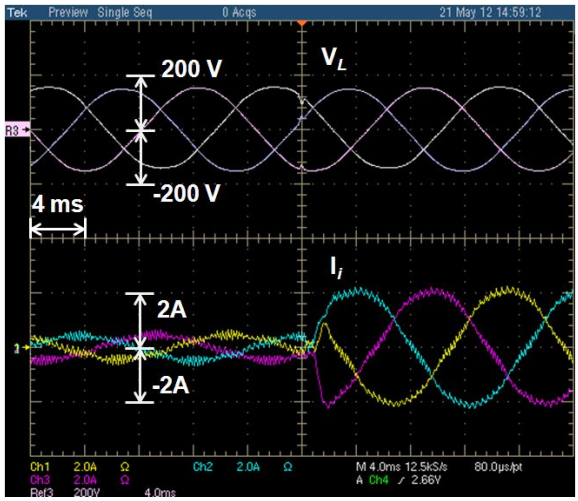

(a)

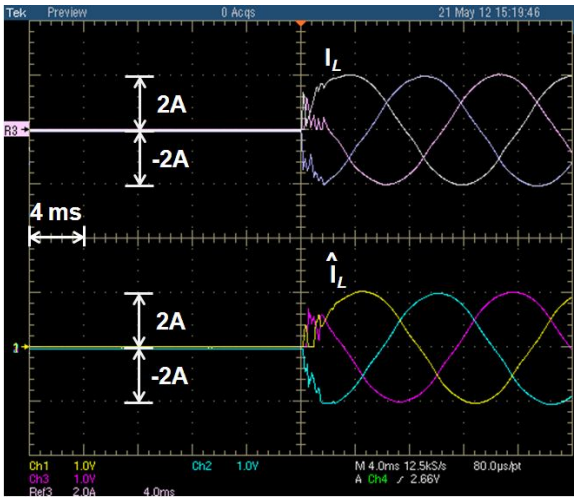

(b)

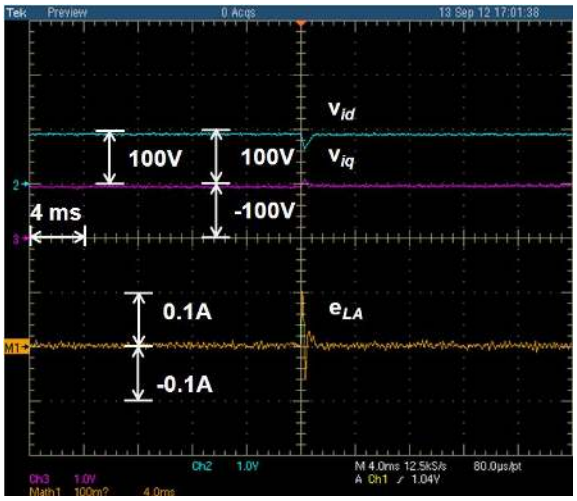

(c)

Fig. 15. Experimental results of the proposed control scheme under Case 1 for a 450 VA unit (Balanced resistive load: 0% to 100%). (a) Load output voltages ($\mathbf{V}_L$) and inverter phase currents ($\mathbf{I}_i$). (b) Load phase currents ($\mathbf{I}_L$) and estimated load currents ($\hat{\mathbf{I}}_L$). (c) Control inputs (v_{id}, v_{iq}) and load current error (e_{LA}).

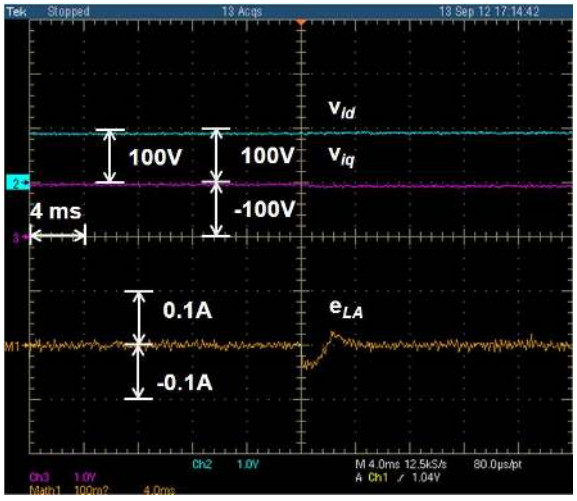

(c)

Fig. 16. Experimental results of the proposed control scheme under Case 2 for a 450 VA unit (Balanced resistive load: 100% to 0%). (a) Load output voltages ($\mathbf{V}_L$) and inverter phase currents ($\mathbf{I}_i$). (b) Load phase currents ($\mathbf{I}_L$) and estimated load currents ($\hat{\mathbf{I}}_L$). (c) Control inputs (v_{id}, v_{iq}) and load current error (e_{LA}).

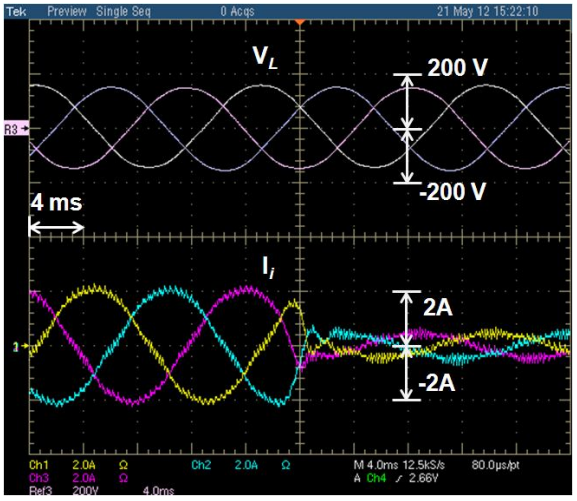

(a)

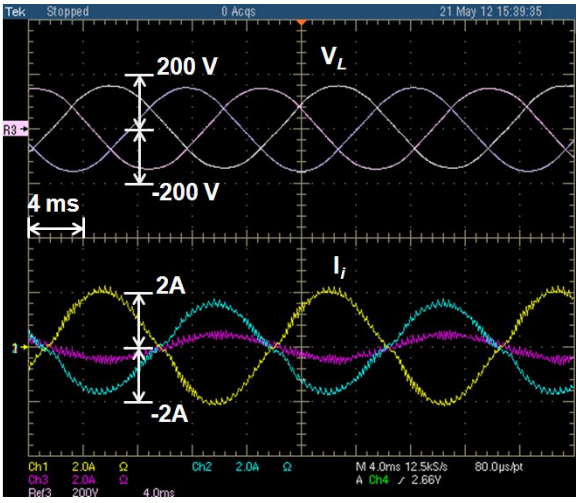

(a)

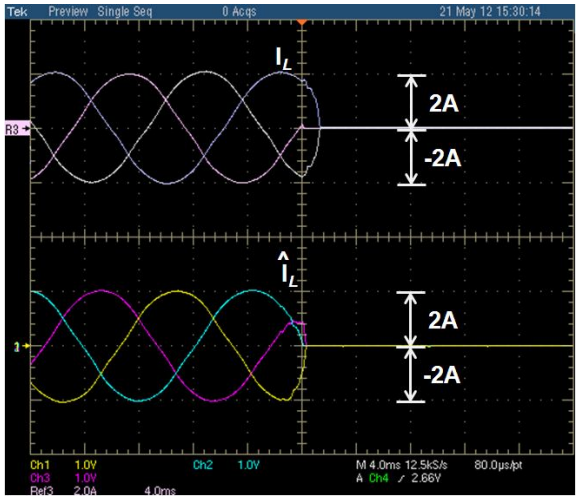

(b)

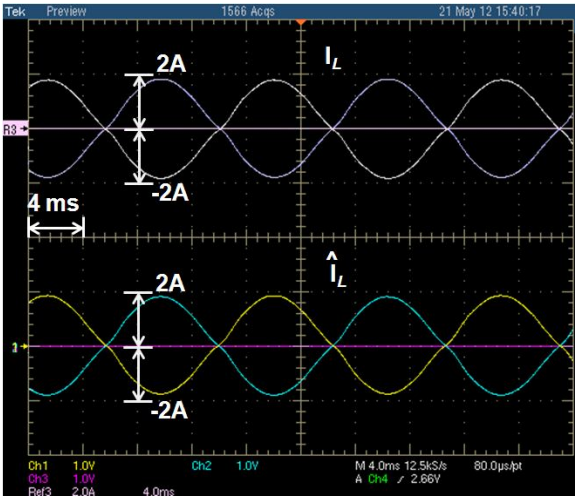

(b)

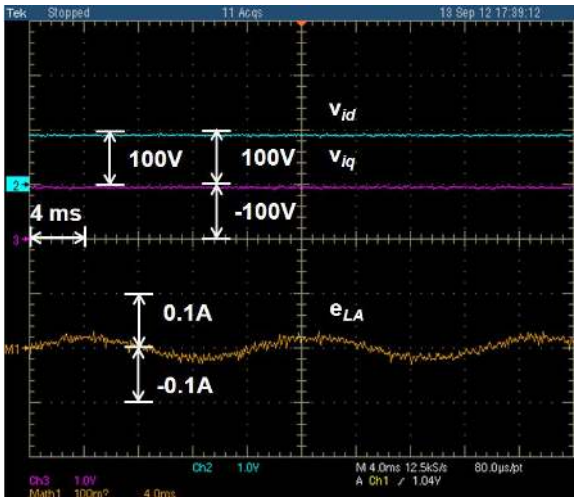

(c)

Fig. 17. Experimental results of the proposed control scheme under Case 3 for a 450 VA unit (Unbalanced resistive load: phase *C* opened). (a) Load output voltages ($\mathbf{V}_L$) and inverter phase currents ($\mathbf{I}_i$). (b) Load phase currents ($\mathbf{I}_L$) and estimated load currents ($\hat{\mathbf{I}}_L$). (c) Control inputs (v_{id}, v_{iq}) and load current error (e_{LA}).

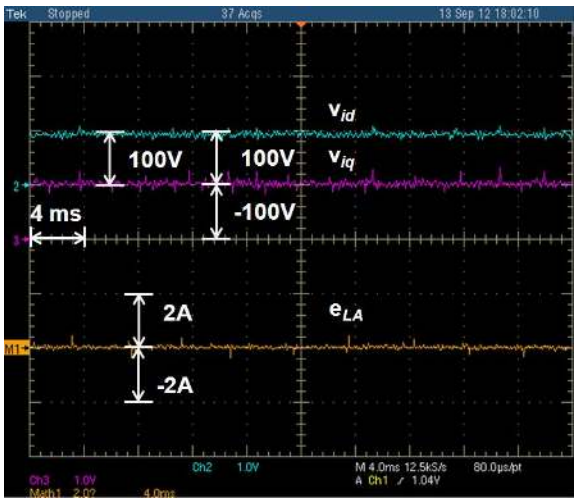

(c)

Fig. 18. Experimental results of the proposed control scheme under Case 4 for a 450 VA unit (Nonlinear load with crest factor 1.52:1). (a) Load output voltages ($\mathbf{V}_L$) and inverter phase currents ($\mathbf{I}_i$). (b) Load phase currents ($\mathbf{I}_L$) and estimated load currents ($\hat{\mathbf{I}}_L$). (c) Control inputs (v_{id}, v_{iq}) and load current error (e_{LA}).

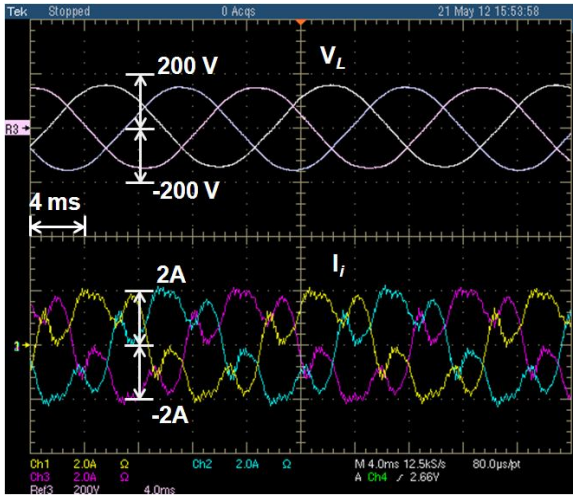

(a)

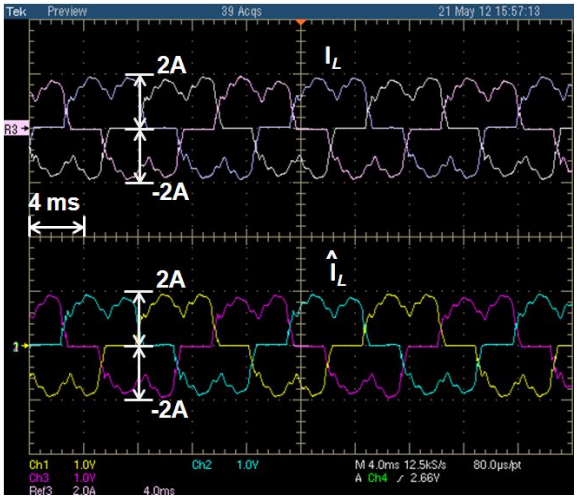

(b)

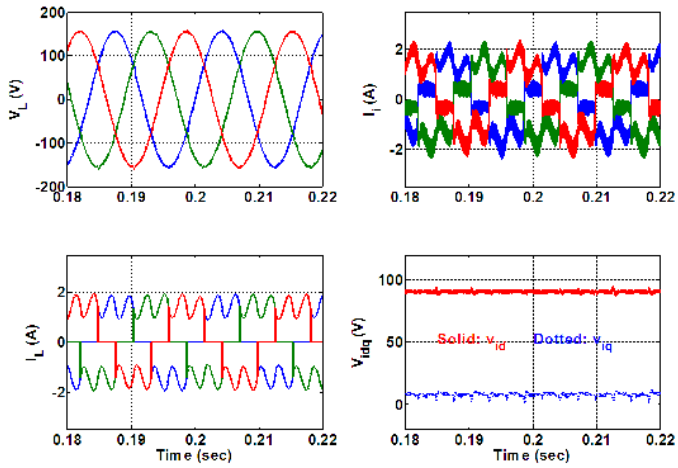

Fig. 19. Simulation results of the FL-MIMO control method under Case 4 for a 450 VA unit (Nonlinear load with crest factor 1.59:1).

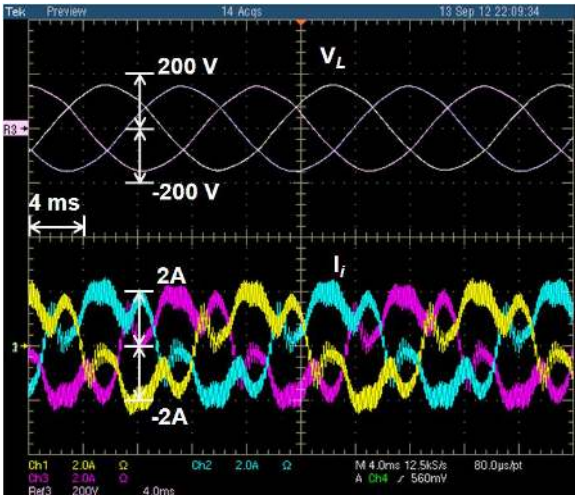

(a)

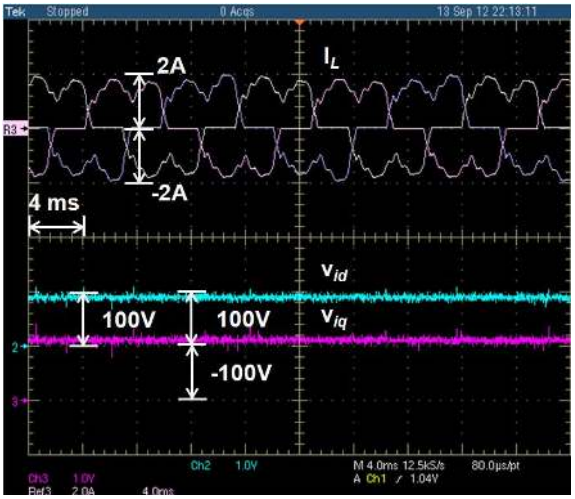

(b)

Fig. 20. Experimental results of the FL-MIMO control method under Case 4 for a 450 VA unit (Nonlinear load with crest factor 1.52:1). (a) Load output voltages ($\mathbf{V}_L$) and inverter phase currents ($\mathbf{I}_i$). (b) Load phase currents ($\mathbf{I}_L$) and control inputs (v_{id}, v_{iq}).

VI. Conclusions

In this paper, an adaptive voltage controller was proposed for a three-phase PWM inverter of standalone DGSs. Load current information was estimated by a fourth-order optimal observer. The stability of the proposed controller and observer was analytically proven by applying Lyapunov stability theory. This adaptive control strategy can achieve more stable output voltage and lower THD than the FL-MIMO control scheme under sudden load change, unbalanced load, and nonlinear load. The effectiveness and feasibility of the proposed control strategy were verified through various simulation and experimental results.

References

[1] F. Blaabjerg, R. Teodorescu, M. Liserre, and A. V. Timbus, "Overview of control and grid synchronization for distributed power generation systems," *IEEE Trans. Ind. Electron.*, vol. 53, no. 5, pp. 1398–1409, Oct. 2006.

[2] A. Mirnaser, "Control of an islanded distributed energy resource unit with load compensating feed-forward," in *IEEE Power Energy Society General Meeting (PES'08)*, Ontario, Canada, Aug. 2008, pp.1-7.

[3] K. L. Nguyen, D. J. Won, S. J. Ahn, and I. Y. Chung, "Power sharing method for a grid connected microgrid with multiple distributed generators," *J. Elect. Eng. Technol.*, vol. 7, no. 4, pp. 459-467, Jul. 2012.

[4] H. C. Seo and C. H. Kim, "Analysis of stability of PV system using the eigenvalue according to the frequency variation and requirement of frequency protection," *J. Elect. Eng. Technol.*, vol. 7, no. 4, pp. 480-485, Jul. 2012.

[5] I. S. Bae and J. O. Kim, "Phasor discrete particle swarm optimization algorithm to configure micro-grids," *J. Elect. Eng. Technol.*, vol. 7, no. 1, pp. 9-16, Jan. 2012.

[6] H. Karimi, E. J. Davision, and R. Iravani, "Multivariable servomechanism controller for autonomous operation of a distributed generation unit: design and performance evaluation," *IEEE Trans. Power Syst.*, vol. 25, no. 2, pp. 853–865, May 2010.

[7] U. Borup, P. N. Enjeti, and F. Blaabjerg, "A new space-vector-based control method for UPS systems powering nonlinear and unbalanced loads," *IEEE Trans. Ind. Appl.*, vol. 37, no. 6, pp. 1864–1870, Nov./Dec. 2001.

[8] T. S. Lee, S. J. Chiang, and J. M. Chang, "H_∞ loop-shaping controller designs for the single-phase UPS inverters," *IEEE Trans. Power Electron.*, vol. 16, no. 4, pp. 473–481, Jul. 2001.

[9] G. Escobar, A.M. Stankovic, and P. Mattavelli, "An adaptive controller in stationary reference frame for d-statcom in unbalanced operation," *IEEE Trans. Ind. Electron.*, vol. 51, no. 2, pp. 401–409, Apr. 2004.

[10] P. Mattavelli, G. Escobar, and A. M. Stankovic, "Dissipativity-based adaptive and robust control of UPS," *IEEE Trans. Ind. Electron.*, vol. 48, no. 2, pp. 334–343, Apr. 2001.

[11] R. Escobar, A. A. Valdez, J. Leyva-Ramos, and P. Mattavelli, "Repetitive-based controller for a UPS inverter to compensate unbalance and harmonic distortion," *IEEE Trans. Ind. Electron.*, vol. 54, no. 1, pp. 504–510, Feb. 2007.

[12] D. E. Kim and D. C. Lee, "Feedback linearization control of three-phase UPS inverter systems," *IEEE Trans. Ind. Electron.*, vol. 57, no. 3, pp. 963–968, Mar. 2010.

[13] A. Houari, H. Renaudineau, J. P. Pierfedrici, and F. Meibody-Tabar, "Flatness based control of three phase inverter with output LC filter," *IEEE Trans. Ind. Electron.*, vol. 59, no. 7, pp. 2890–2897, Jul. 2012.

[14] H. Deng, R. Oruganti, and D. Srinivasan, "Analysis and design of iterative learning control strategies for UPS inverters," *IEEE Trans. Ind. Electron.*, vol. 54, no. 3, pp. 1739–1751, Jun. 2007.

[15] P. Cortés, G. Ortiz, J. I. Yuz, J. Rodrisguez, S. Vazquez, and L. G. Franquelo, "Model predictive control of an inverter with output *LC* filter for UPS applications," *IEEE Trans. Ind. Electron.*, vol. 56, no. 6, pp. 1875–1883, Jun. 2009.

[16] K. H. Ahmed, A. M. Massoud, S. J. Finney, and B. W. Williams, "A modified stationary reference frame-based predictive current control with zero steady-state error for LCL coupled inverter-based distributed generation systems," *IEEE Trans. Ind. Electron.*, vol. 58, no. 4, pp. 1359–1370, Apr. 2011.

[17] H. Karimi, A. Yazdani, and R. Iravani, "Robust control of an autonomous four-wire electronically-coupled distributed generation unit," *IEEE Trans. Power Deliv*. vol. 26, no. 1, pp. 455-466, Jan. 2011.

[18] T. L. Tai and J. S. Chen, "UPS inverter design using discrete-time sliding-mode control scheme," *IEEE Trans. Ind. Electron.*, vol. 49, no. 1, pp. 67–75, Feb. 2002.

[19] O. Kukrer, H. Komurcugil, and A. Doganalp, "A three-level hysteresis function approach to the sliding-mode control of single-phase UPS inverters," *IEEE Trans. Ind. Electron.*, vol. 56, no. 9, pp. 3477–3486, Sep. 2009.

[20] H. Komurcugil, "Rotating sliding line based sliding mode control for single-phase UPS inverters," *IEEE Trans. Ind. Electron.*, vol. 59, no. 10, pp. 3719–3726, Oct. 2012.

[21] R. J. Wai and C. Y. Lin, " Dual active low-frequency ripple control for clean-energy power-conditioning mechanism," *IEEE Trans. Ind. Electron.*, vol. 58, no. 11, pp. 5172–5185, Nov. 2011.

[22] M. Dai, M. N. Marwali, J. W. Jung, and A. Keyhani, "A three-phase four-wire inverter control technique for a single distributed generation unit in island mode," *IEEE Trans. Power Electron*., vol. 23, no. 1, pp. 322-331, Jan. 2008.

[23] M. N. Marwali and A. Keyhani, "Control of distributed generation systems–part I: voltages and currents control," *IEEE Trans. Power Electron.*, vol. 19, no. 6, pp. 1541-1550, Nov. 2004.

[24] F. L. Lewis, C. T. Abdallah, and D. M. Dawson, *Control of Robot Manipulators*, New York: MacMillan, 1993.

[25] K. J. Astrom and B. Witternmark, *Computer-Controlled Systems–Theory and Design*, Englewood Cliffs, New Jersey: Prentice-Hall Inc., 1990.

[26] B. Shahian and M. Hassul, *Control System Design Using Matlab*, Englewood Cliffs, New Jersey: Prentice-Hall Inc., 1993.

Ton Duc Do (S'12) received the B.S. and M.S. degrees in electrical engineering from Hanoi University of Technology, Hanoi, Vietnam in 2007 and 2009, respectively. From 2008 to 2009, he worked at Water Resources University, Hanoi, Vietnam, as a lecturer. He is currently pursuing the Ph.D. degree in the Division of Electronics and Electrical Engineering, Dongguk University, Seoul, Korea. His research interests are in the field of electric machine drives and control of distributed generation systems using renewable energy sources.

Viet Quoc Leu (S'12) received the B.S. and M.S. degrees in electrical engineering from Hanoi University of Technology, Hanoi, Vietnam in 2006 and 2008, respectively. He is currently pursuing the Ph.D. degree in the Division of Electronics and Electrical Engineering, Dongguk University, Seoul, Korea. His research interests are in the field of DSP-based electric machine drives and control of distributed generation systems using renewable energy sources.

Young-Sik Choi received the B.S. degree in electrical engineering from Dongguk University, Seoul, Korea in 2009. He is currently pursuing the Ph.D. degree in the Division of Electronics and Electrical Engineering, Dongguk University, Seoul, Korea. His research interests are in the field of electric machine drives based on microprocessor and control of distributed generation systems using renewable energy sources.

Han Ho Choi (M'03) received the B.S. degree in control and instrumentation engineering from Seoul National University, Seoul, Korea, in 1988, and the M.S. and Ph.D. degrees in electrical engineering from Korea Advanced Institute of Science and Technology, Daejeon, Korea, in 1990 and 1994, respectively. From 1994 to 1998, he was a Team Leader with the Advanced Technology Laboratory, DaeWoo Electrical Company. He is currently with the Division of Electronics and Electrical Engineering, Dongguk University, Seoul, Korea. He spent his sabbatical with the Department of Electrical and Computer Engineering, Cal Poly Pomona. He teaches introductory electrical engineering courses on microprocessors, robotics, sensors, and instrumentation engineering. His research interests include linear-matrix-inequality-based control system design, microprocessor-based control systems, and variable structure systems.

Jin-Woo Jung (S'97–M'06) received the B.S. and M.S. degrees in electrical engineering from Hanyang University, Seoul, Korea in 1991 and 1997, respectively, and the Ph.D. degree in Electrical and Computer Engineering from The Ohio State University, Columbus, Ohio, USA, in 2005. From 1997 to 2000, he was with the Digital Appliance Research Laboratory, LG Electronics Co., Ltd., Seoul, Korea. From 2005 to 2008, he worked at the R&D Center and PDP Development Team, Samsung SDI Co., Ltd., Korea, as a senior engineer. Since 2008, he has been an Associate Professor with the Division of Electronics and Electrical Engineering, Dongguk University, Seoul, Korea. His current research interests are in the area of electric machine drives, control of distributed generation systems using renewable energy sources (wind turbines/fuel cells, solar cells), design and control of power converters, and driving circuits and driving methods of ac plasma display panels (PDP).